Simultaneous measurements of water impact on a two-dimensional body

1997 Fluid Dyn. Res. 19 125

(http://iopscience.iop.org/1873-7005/19/3/A01)

ELSEVIER

Fluid Dynamics Research 19 (1997) 125–148

FLUID DYNAMICS RESEARCH

Simultaneous measurements of water impact on a two-dimensional body

Ming-Chung Lin*, Li-Der Shieh

Department of Naval Architecture & Ocean Engineering, National Taiwan University, 73, Chow-Shan Road, Taipei, Taiwan, ROC

Received 19 January 1996; revised 16 April 1996; accepted 9 August 1996

Abstract

This study utilizes a high-speed charge coupled device (CCD) camera as the data acquisition system to simultaneously measure the pressure and flow field. The measurement system can be triggered by an external optical sensor, to obtain the free surface and pressure variations in each time step of the initial stage of water impact. The whole field image was observed by a high-speed area scan sensor camera. Almost no interval between photographing moving objects was allowed owing to the extremely short transfer time and high exposure sensitivity of the camera. Following image transfer, this characteristic and the hardware computational function of a video card not only allowed for binarization, accumulative addition but we could also quickly identify the track of a moving object and obtain the image and numerical data which we needed. Moreover, the flow characteristics are observed via a flow following "seeding" particles, and the digital particle tracking velocimeter (DPTV) so that the flow field velocity distribution can be measured.

Keywords: Cylinder; Flat-bottom body; Water impact; Simultaneous measurements; DPTV

Nomenclature

a	acceleration
α	radial angle of immersed circular cross-section
θ	radial angle (between measurement position and peak point)
ρ_w	mass density of fluid
g	gravity acceleration
h, h_0	thickness of air layer
H_0	dropping height
l	half-width of a flat-bottom body

* Corresponding author.

PII S0169-5983(96)00033-0

M	mass of falling body per unit length
m	added mass of falling body per unit length
P, P_0	impact pressure
P_{max}	maximum impact pressure
q	external force acting upon falling body
r	the ratio of entry depth and the radius of cylinder
R	cylinder radius
t	time
t_0	beginning of exposure time
t_f	frame sampling and readout time
t_t	transfer time
U_1	the velocity along the X direction at unknown grid point
U_K	the velocity along the X direction after recognition
V	velocity in general
V_0	impact velocity
V_1	the velocity along the Y direction at unknown grid point
V_K	the velocity along the Y direction after recognition
X_K	the local coordinate related to the unknown grid point, along the X direction
X, X_0	movement distance
y	entry depth of cylinder
Y_K	the local coordinate related to the unknown grid point, along the Y direction

1. Introduction

A ship traveling at high speed or in heavy sea frequently has its bow and bottom damaged by high pressure caused by impact with and detachment from the water surface. Considerable impact may also occur when large waves hit the cross member or deck plate of an offshore structure within the splash zone. Many engineering cases require consideration of impact pressure, the movement of objects and change of the flow field. For instance, spacecrafts falling into water upon return, underwater weapons (e.g., torpedoes, anti-subrockets and missiles) and underwater vehicles (e.g., lifeboats) upon launch are struck by enormous impact pressure which causes violent water surface variations, thereby influencing the object's movement. If the wavelength is significantly longer than the object diameter, the water surface can be defined as a calm water surface. These complicated phenomena are generally simplified into two-dimensional cross-section problems with wedge-cylinder or flat-bottom body impacting the calm water surface as free-falling bodies and then the motion is analyzed and the physical mechanism discussed. Previous works involving water impact have focused primarily on impact pressures, of which those caused by a blunt body (flat-bottom body, cylinder) are the most special. This study examines the impact pressure and the flow field on a calm water surface.

Von Karman (1929) and Wagner (1932) first analyzed cylinder impact with a water surface, using equivalent plates to represent impact objects and solving the impact pressure problems. Wagner's theory that the water surface rises along the cylinder surface is generally considered to be closer to the actual situation. The water impact on a cylinder has received only limited experimental

attention, the most important result being that of Campbell and Weynberg (1980). However, they did not include the variation of water surface during impacts. In addressing this concern, Greenhow and Lin (1983) took a series of photographs of cylinder entry and exit from the water surface. Thereafter, Greenhow (1988) solved the water surface variation and impact force problems via Cauchy's integration theorems and also used Lagrange's approach. However, they did not simultaneously measure the pressure and flow field. As a consequence, there is no satisfactory understanding of the relationship between impact pressure and flow field variation.

Water impact on a flat-bottom body is the most special. To our knowledge, no complete descriptions of water impact on a flat-bottom body are available. There are many papers (Fujita, 1953; Chuang, 1966; Verhagen, 1967; Gerlach, 1968) which indicate that the factors influencing the impact pressure include impact velocity, weight, bottom area, and bottom edge. The air layer effect (or cushion effect) is thought to be the source of those factors. However, there is no satisfactory understanding of the air layer damping mechanism. Chuang (1966) used the assumption that the oscillation period of impact pressure is equal to twice the model width divided by the sound speed through air. Whitmen (1973) used the method of dimensional analysis to derive a piston type "trapped air" impact model to describe its occurrence in Gerlach's experiment. Koehler and Kettleborough (1977) and Ng and Kot (1992) applied the concepts of finite difference and constant volume of fluid (VOF) to solve the Navier–Stokes equations for a two-density fluid. They attained the initial stage of wave formation and non-dimensional pressure coefficient for the case of a flat-bottom body impacting the water surface. Efforts such as Whitmen's dimensional analysis and Koehler's and Ng's numerical simulation of water surface variation have clearly suggested a mechanism; however, no simultaneous experimental data were provided.

The main reasons why the impact pressure and fluid field could not be simultaneously measured in past experiments include the following:

1. Previously, a complicated instrumental design was required to obtain instant impact pressure. Also, controlling the measurement timing was relatively difficult.
2. A conventional mechanical high-speed camera could not directly determine the relationship in time with the mechanical (pressure, acceleration) data.

To overcome these difficulties, this study set up a set of experimental equipment to simultaneously measure pressure, acceleration and flow fields, thereby allowing for an investigation of the complete phenomenon of a blunt body (flat-bottom body, cylinder, etc.) slamming the water surface.

2. Experimental design and method

2.1. Experimental plan

Fig. 1 illustrates the experimental layout. When the pressure valve is released, the model over the experiment rack falls freely. It triggers an optical sensor to switch on a data acquisition card of the personal computer which automatically records the variations of acceleration and of pressure during movement. Simultaneously, the optical sensor also switches on a high-speed camera to capture images of the flow field. An experiment involving the water impact of wave was performed in a 20 m long, 0.8 m wide, 0.6 m deep wave tank in which a 4 m long, 0.2 m wide experimental

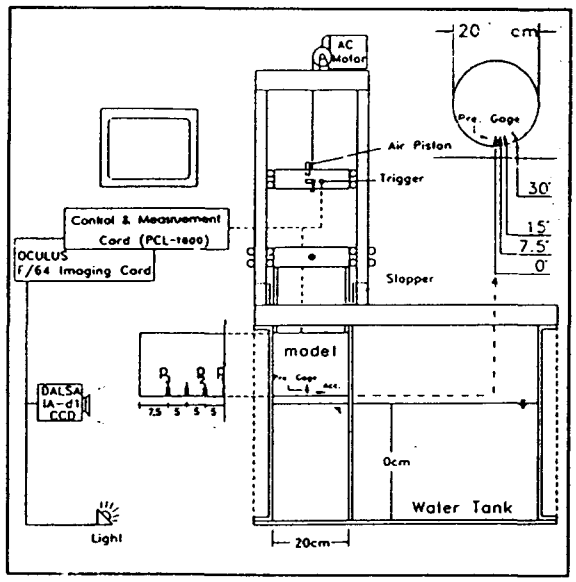

Fig. 1. Experimental layout.

channel was partitioned off by acrylic boards. The optical sensor's reaction time was 140 μs. The accelerometer was a KYOWA model ASW-20A. The pressure gauge was a KYOWA model PGM-2KC with diameter of 5.5 mm; the non-linearity and hysteresis were smaller than 1.5% RO (rated output), the natural frequency exceeded 24 kHz, and the highest measurement pressure was 2000 g/cm^2. Measurement and control were executed on a 486PC with a grabber card having a 200 kHz 12-bit analog/digital transfer rate.

2.2. *Video sampling theory and simultaneous measurement method*

The CCD camera used in the measuring system operated at a high output rate of 16 MHz. It uses a high-sensitivity area array image sensor, capable of eliminating the discontinuities and errors caused by general linear image sensors while photographing objects moving at high velocity. Fig. 2 shows the operating layout of the sensors. The sensor area remains exposed to accumulate electrical charge within the sampling time (t_f). Next, the electrical charges are transferred to a storage area with an extremely short transfer time (t_t). Finally, these charges pass through the transfer gate sequentially and are converted to video signals for output. Fig. 3 exhibits the relationship between time and signals during the above processes. The camera completes the sampling, storage and transformation following the timing signal MCLK provided by the video card. Video signal outputs are -1–0.02 V analog signals during the sampling time (t_f), representing the intensity of each pixel. The outputs within the transferring time (t_t) are $+0.15$ V TTL signals, and are used to recognize the pictures displayed on the video card. This study simultaneously connected the image signals (out of camera), pressure signals and acceleration signals to the A/D grabber card. The time lags of the pressure gauge and accelerometer are smaller than the

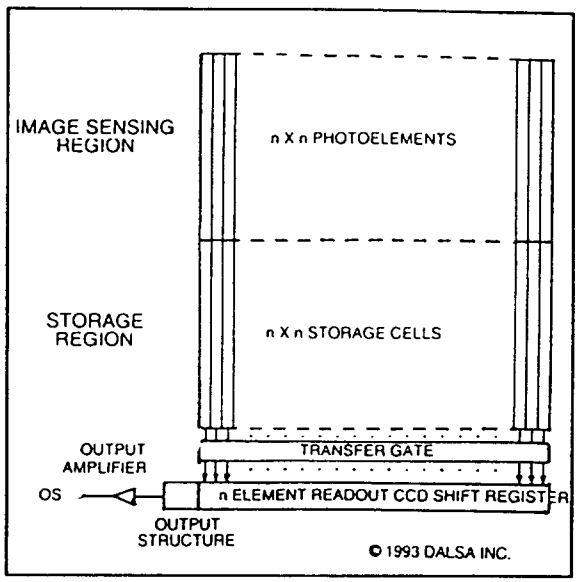

Fig. 2. Block diagram of image sensor.

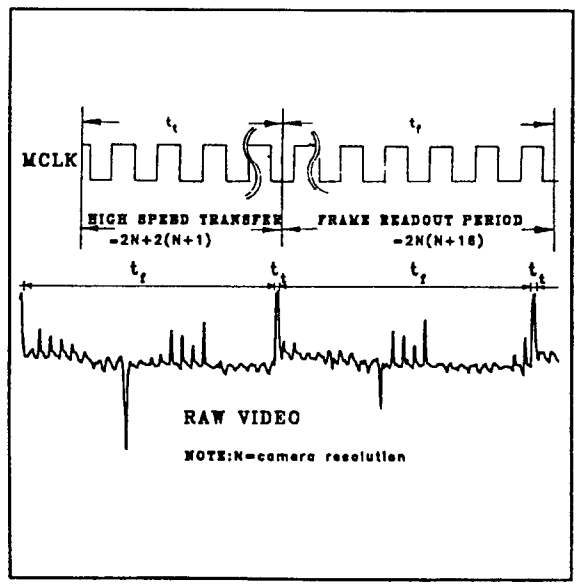

Fig. 3. Timing of image signals.

picture exposure time ($t_f + t_t$). Therefore, the time lags can be negative. These images and pressure were recorded simultaneously. This experiment uses sensors with 256×256 resolution; the transferring time is 0.104 ms, the sampling time is 5.58 ms, and 175 images can be taken per second.

2.3. *Image processing*

Analog video signals are first sent to the video card in a personal computer. The water surface wave formation, body displacement, and air layer thickness can be obtained via the real time processing functions of the video card. Fig. 4 illustrates the image signal procedure method. In this figure, the gray scales of the two segment tracks are set to 10 and 20, respectively. The characteristics of the moving object can be obtained by accumulative addition as follows: (1) body outline and body size (gray scale of 30); (2) body movement distance and velocity; (3) point A moves to point B. The functioning and principles of the video card are briefly explained as follows:

(1) *Input and storage*: The 40 Mbyte/s analog-to-digital converters on the video card convert the video signals to 8-bit digital signals, representing 256 gray levels, and then store them in a VRAM. These signals are then transferred through the input look-up table (ILUT) to be converted to data with time axis and coordinate information, and can be processed in real time to satisfy various requirements.

(2) *Binarization*: The gray scale is set at the boundary of observed objects to a high-pass value. All of the noises with values lower than the high-pass one are filtered out. ILUT's binarization can clearly recognize and outline the objects.

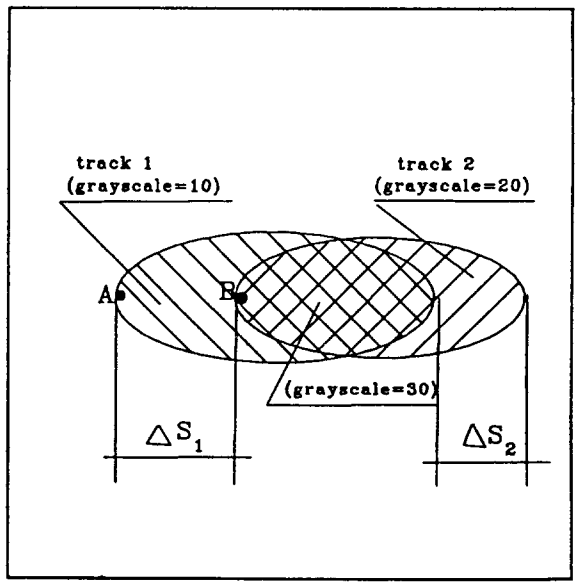

Fig. 4. Image signals procedure.

(3) *Accumulative addition*: The video card provides a 40 Mbyte/s IP engine for accumulative additions. Following these additions, binary video signals can provide different gray scales representing the tracks of the body in different time stages.

(4) *Digital particle tracking velocimeter (DPTV)*: In this study, the flow field characteristics are observed by following "seeding" particles. Four-segment color codes with four accumulative additions are selected. Therefore the middle two color codes can be recognized, and particle path errors can be eliminated. Retrieving the velocity vectors from the particle track requires assistance from the floating point digital processor on the video card's TM34020 GSP (graphic signal processor). Therefore, the processes of thinning, velocity vector recognition, inner insertion, and reconstruction can be performed, as described below:

(1) *Thinning*: The ideal state of four-segment color code lines should be line segments with equal widths. Dividing the skeleton length by the exposure time yields the velocity. The direction of the skeleton is the particle's movement direction. This work adopts the SPTA (safe-point thinning algorithm) of Naccalhe and Shinghal (1984) to perform track thinning of four-segment color codes.

(2) *Recognition*: After applying thinning procedures to the lines, relative theories and timing code of images are also applied to recognize the vector information of those lines.

(3) *Velocity distribution*: The track's approximate equations can be obtained by applying the second-order dispersion method of Khalighi and Lee (1989) to the particle positions along the line tracks. The length can be obtained by integration along the track. Next, the average velocity can be obtained by dividing the length by exposure time. The tangent direction at the center of the track is the direction of movement.

(4) *Interpolation processing*: After retrieving a certain amount of vectors, the interpolation equation of Imaich and Ohmi (1983) can be used.

(5) *Reconstruction and output*: Results obtained from the above-mentioned procedures can either be directly output on a monitor screen or saved as data files in other formats.

(6) *Measurement uncertainty*: The precision of DPTV measurement is determined by the resolution of the CCD camera and number of pixels for a particle diameter. The more particle traces pass through the pixel the more accurate. In our (image) system and experiment condition which could distinguish the particle velocity of 0.15–2 m/s, the mean deviation is 8%.

2.4. Experimental conditions

Two acrylic models having a thickness of 20 cm and a weight of 12.5 kg were used in this study. The flat-bottom body model has a width of 45 cm and the cylinder model has a diameter of 20 cm. The pressure gauge is installed at the center, 5 cm from the center and 15 cm from the center of the flat-bottom and installed at the circular center angles of the cylinder $\theta = 0°$, 7.5°, 15°, 30° as shown in Fig. 1. Next, impact experiments were performed at dropping heights of 1, 3, 5, 10, 15, 20 cm, respectively. The comparison error between dropping time and acceleration data was 5%. Therefore, we applied $V = (2gh)^{1/2}$ as the impact velocity. The experiment was performed at a high sampling frequency of 25 kHz. Pressure records and water surface variation records were obtained several times, and had very good repeatability. Although the camera speed was 175 pictures per second, the variation could be obtained by performing the experiment several times. A more thorough understanding of the physical appearance of pressure and water surface variation could also be obtained. The window size for viewing the process of creating an air layer was different from that for viewing the water surface variation. Therefore, 8.5 and 16 mm lenses were used separately.

3. Experimental results

To describe the mechanism of water impact, some of the results were displayed as raw data and some as dimensionless values. The dimensionless acceleration, entry depth and impact pressure are expressed by a/g, y/R and $p/\frac{1}{2}\rho_w V_0^2$, respectively. Here g is the gravity acceleration and ρ_w the mass density of the fluid. The impact pressure occurs in a very short time. Thus, the dimensionless time could be scaled as R/V_0 (V_0: impact velocity; R: radius of the cylinder) or D/V_0 (D: width of the flat-bottom body) in different models. However, this paper uses dimensional time with the same interval as video images to make the comparisons easier.

3.1. Water impact of the flat-bottom body

3.1.1. Description of air layer creation

Experimental results indicated that the air layer and pressure variation of the flat-bottom body impacting water surface corresponded well under falling heights of 3, 5, 10, 15, and 20 cm. Fig. 5 summarizes the results of the test for a falling height of 10 cm performed twice. The upper numbers of Figs. 5a and 5b mark the related image record. When the flat-bottom body was close to the water surface, the air in the air layer flowed outside. Immediately prior to contact with the water surface, a slight amount of water mixed with air went out of the flat-bottom (Fig. 5-1). At this time, the pressure rose slightly (Fig. 5a). When the flat bottom contacted the water surface, spray splashed out around the flat bottom. Simultaneously, bubbles formed near the edge (Figs. 5-2 and 5-3).

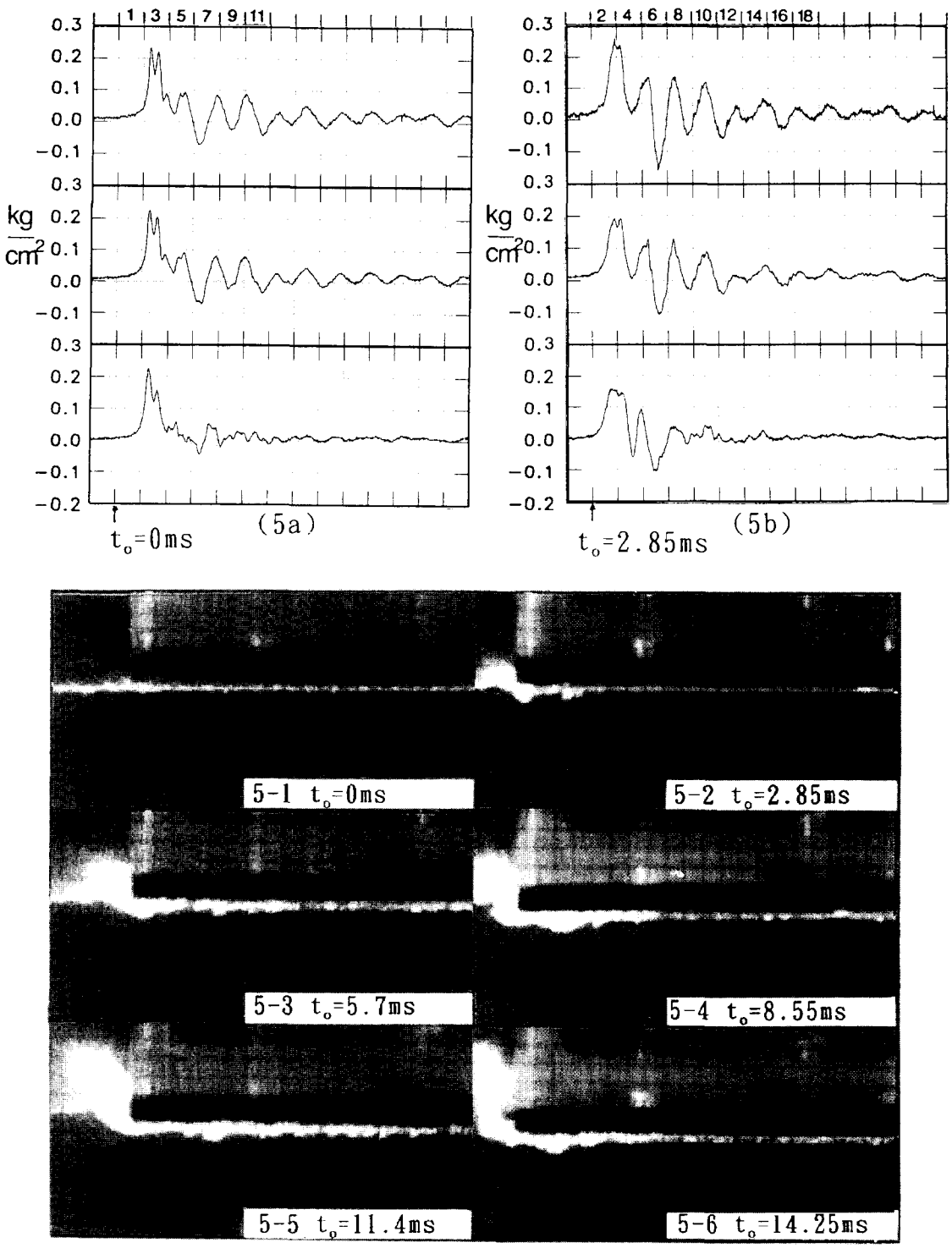

Fig. 5. Impact pressure and acceleration records and air layer video picture (falling height 10 cm, t_0: beginning of the exposure, ms = 10^{-3} s).

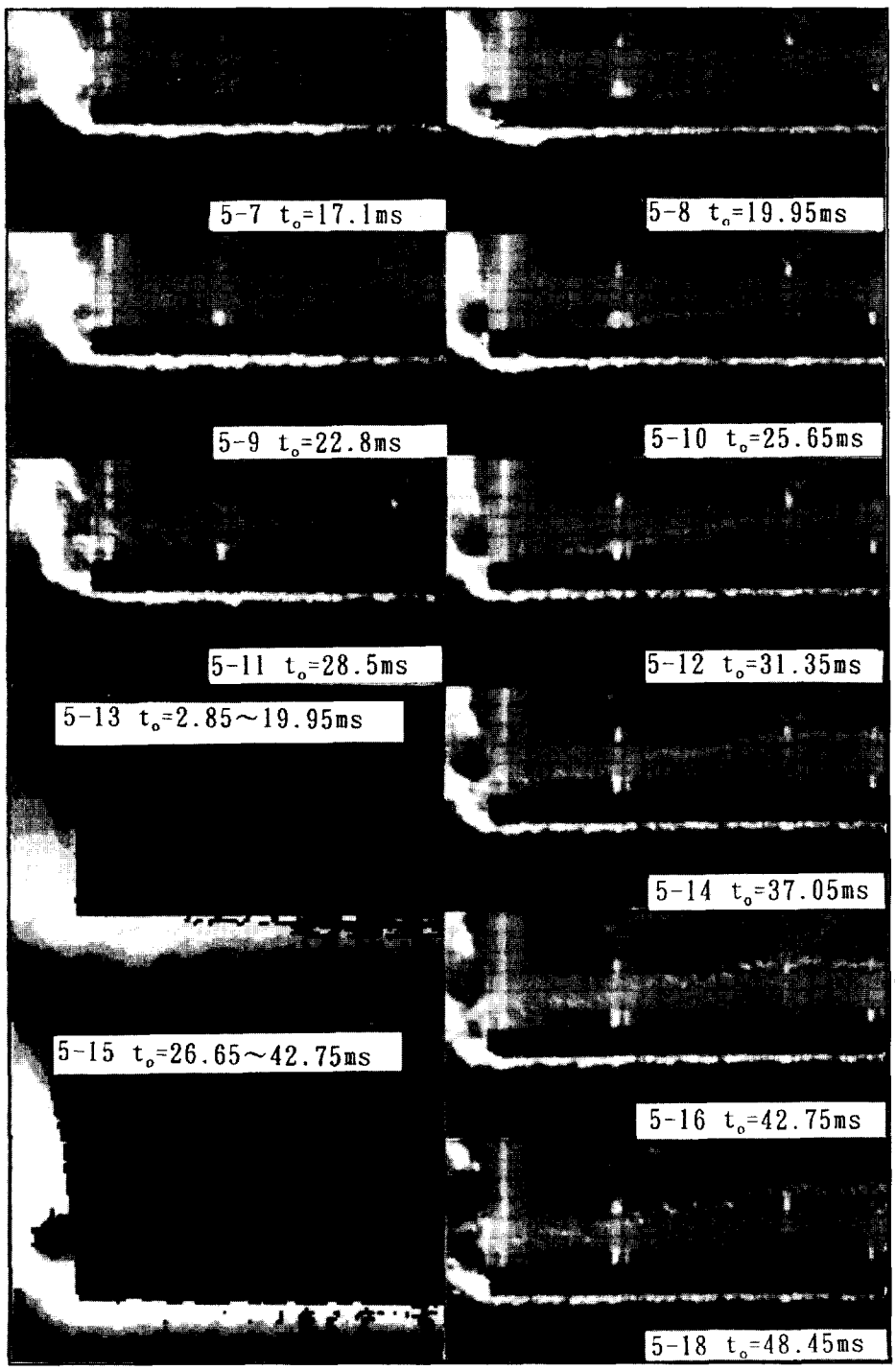

Fig. 5. Continued.

The flat-bottom body continued to fall and bubbles were generated from the edge to the bottom's center (Figs. 5-4 and 5-5). P1 and P2 became oscillations of consistent wave form. Figs. 5a and 5b correspond well with each other. However, P3 did not have such a regular oscillation after the pressure achieved its peak value. According to Fig. 5a, after the pressure achieved its peak value, the pressure of the impact position of Fig. 5-5 obviously disappeared. On the other hand, the pressure in Fig. 5b still had three regular oscillations, while the impact position of Fig. 5-8 also obviously disappeared. From these figures, we can infer that the pressure disappears as bubbles spread out to P3. The bubbles occupied the entire bottom area as the flat-bottom body continued falling (Figs. 5-7 and 5-8). No impact pressure arose, even though a disappearing phenomenon occurred.

Figs. 5-13 and 5-15 are formed by binarization and addition of 5-2, 4, 6, 8 and 5-10, 12, 14, 16, respectively. The trace of bubbles moving out and the water spray are obvious. Analyzing the images obtained from different impact velocities reveal that the bubbles' splash speed varies from 40 to 70 cm/s. The center of the flat bottom maintains an air layer until the impact pressure disappears. Additional results indicate that the air layer thickness is 0.2 cm. The results for different impact speeds closely resembled each other.

The above description revealed that the air layer type obtained in this study closely resembles those obtained from the numerical calculations of Ng and Kot (1992, Figs. 6, 8, 10 and 12). Also, the trace of flow speed in the air layer in Ng and Kot (1992, Figs. 8 and 10) indicates that the flow speed around the edge of the flat-bottom body was rapid at the beginning of impact. The slight change in the water surface might account for the fluid spin and the subsequent generation of bubbles.

3.1.2. Variation of impact pressure and acceleration

Fig. 6 compares the variations of impact pressure and acceleration under different impact velocities. At the early stage of impact, acceleration and impact pressure vary consistently. After the first peak appeared, the pressure became negative. The rate of acceleration change increased, but the rate of pressure change remained the same. After about 10×10^{-3} s, the acceleration changed violently. This charge did not correspond to a change in velocity. The acceleration produced the second peak and then oscillated for a period longer than the pressure's oscillation period. Figs. 5-3 and 5-4 display photographs of the impact position of the flat-bottom body. A strong water spray was splashing out. Therefore, the peak value of the second acceleration was caused by the violent change in flow field. By applying FFT analysis to the spectrum, an insufficient amount of sampling time was due to the limited duration of impact pressure. Under different impact speed, Fig. 6 indicates only a slight change in acceleration and pressure oscillation frequency; this change could not be identified by spectrum analysis. Here, only the spectrum for the dropping height of 10 cm was found (Fig. 7). The pressure spectrum had two peaks around 140 and 67 Hz. The peak at 140 Hz had a narrower band and higher energy. The acceleration spectrum also had two peaks around 80 and 140 Hz. However, the energy around 140 Hz was significantly smaller. The characteristic description in the previous section and the above explanation suggest that the peak around 140 Hz might be caused by the existence of an air layer. The fact that the air layer broke up into bubbles from the edge towards the center and then disappeared would account for the reason why the flat-bottom body movement was smaller. Also, the related energy of the acceleration spectrum was smaller. Moreover, the pressure frequency caused by the existence of an air layer was not consistent with the acceleration frequency. In the low-frequency part, the acceleration spectrum was not directly related to that of pressure.

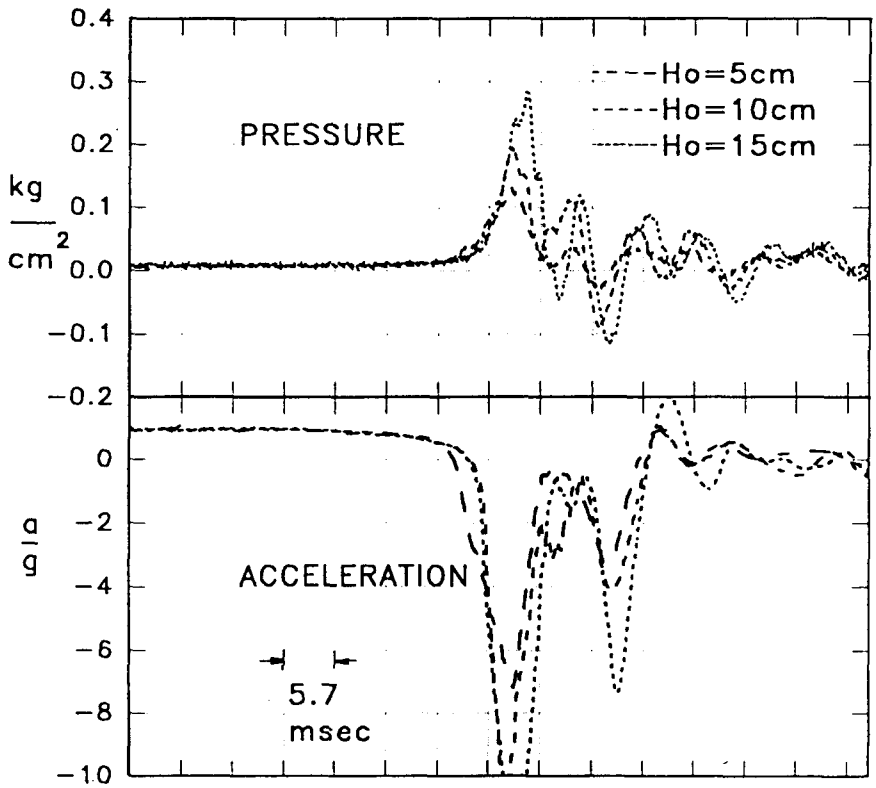

Fig. 6. Impact pressure and acceleration records with various impact velocities.

The dimensionless mean value of the maximum pressure is shown in Table 1 for comparison. This table indicates that higher impact velocity implies lower dimensionless maximum pressure. Moreover, the air layer effect is obvious.

3.1.3. Cause of pressure oscillation

The pressure spectrum has two peaks, at 140 and 67 Hz. According to Chuang's theory, the pressure oscillation period T = double model width/sound speed = 0.00264 s. The frequency at 377 Hz was different from that measured in this study. Therefore, we assume that the oscillation may be caused by compression and expansion of the air layer. The relationship between pressure oscillation frequency and air layer thickness is derived using added mass theory (Appendix A). The air layer thickness is

$$h_0 = \left(\frac{M+m}{Mm}\right)\frac{2lP_0}{4\pi^2 f^2}. \tag{1}$$

Experimental data ($P_0 = 10^5\ \mathrm{N/m^2}$, $M = 62.5$ kg, $l = 0.225$ m) are substituted into the right-hand side of Eq. (1). When the frequency $f = 140$ Hz, the air layer thickness $h_0 = 0.166$ cm, which closely resembles the experimental results. When $f = 67$ Hz, the air thickness becomes 0.72 cm, which is

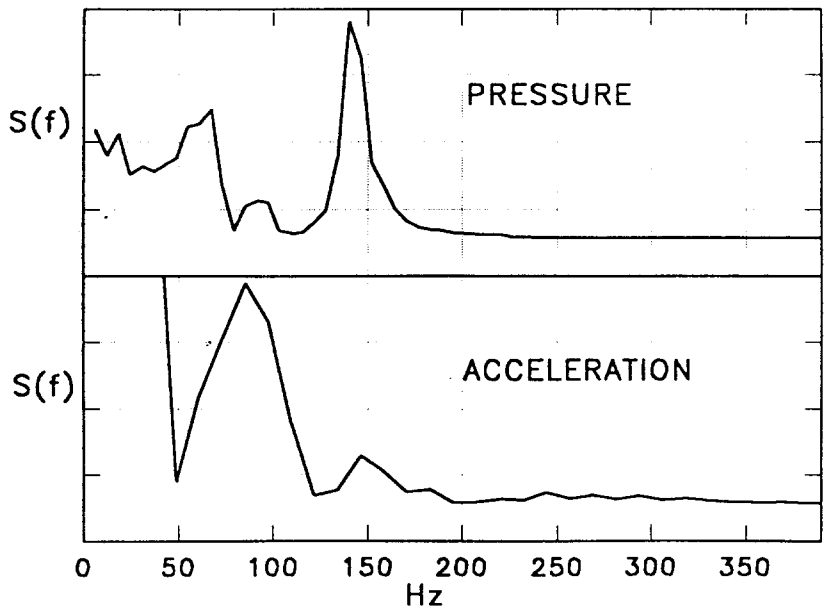

Fig. 7. Impact pressure spectrum and acceleration spectrum (falling height 10 cm).

Table 1
Comparison of dimensionless results at different impact velocities

Impact velocity V_0 (m/s)	0.76	0.99	1.40	1.71	1.98
Pressure coefficient	29.2	29.4	20.2	17.1	15.6

Pressure coefficient $= (P_{max}/\frac{1}{2}\rho V_0^2)$.

quite in contrast with the experimental results. Spectral characteristics can be based on the discussion in the above section. A relationship between water surface vibration and pressure can be derived. We believe that 140 Hz is the oscillation frequency caused by the air layer, while 67 Hz is the frequency caused by the model and fluid.

3.1.4. Discussion

The pressure changes at P1, P2 and P3, as described in the first section, reveal that the vibration duration of impact pressure was longer with the continued presence of the air layer. However, the acceleration record and the spectral analysis indicate that the impact pressure on the flat bottom became smaller after the highest impact pressure occurred. From a physical perspective, pressure oscillation increases partial pressure. However, the average force on the body remains the same. The body movement is affected primarily by the fluid.

Comparing the measurement results of this study with those of Chuang (1966) indicates that the water surface wave formations in both studies are very close, while the oscillation frequency characteristics have an obvious discrepancy. Also, the frequency characteristics found in

Verhagen (1967), Chuang (1979) and Miyamoto (1984) are different from those of Chuang (1966). Therefore, the inference of Chuang (1966) cannot be used in the other models. In this study, the theory of pressure oscillation period and air layer thickness can account for the physical character, but not for the detailed quantitative results. This study has overcome the difficulty of simultaneous fluid field photos and physical measurements. Also, the physical process of a flat-bottom impacting the water surface is adequately described in this study as well. The air layer thickness and its structure could not be further explored owing to the model size and camera resolution.

3.2. Simultaneous measurements of a cylinder under water impact

3.2.1. Displacement of cylinder upon entry into water

Until now, all impact pressure theories and numerical calculations have treated the velocity of impact objects after entry into water as constants. Under this assumption, a similar method can be employed to obtain the solution employing a numerical model for interaction. Fig. 8 compares the theoretical and experimental values of cylinder displacements under various velocities. In this figure, the theoretical values were derived by added mass theory (Appendix B), the experimental values are connecting curves retrieved by reading the coordinates at the gray level changing points in video images, and then performing calculation via the least-squares method. Dotted lines denote the displacements calculated from the theory. This figure clearly indicates that the experimental values for the sample having an impact velocity greater than 98.9 cm/s are close to straight-line movement with constant velocity. However, the samples with lower impact velocity have semi-constant velocity movements. The displacements of experimental values are lower than the calculated values and, therefore, resemble movement with constant velocity. This finding indicates that the cylinder receives a larger impact force than the theoretically calculated value.

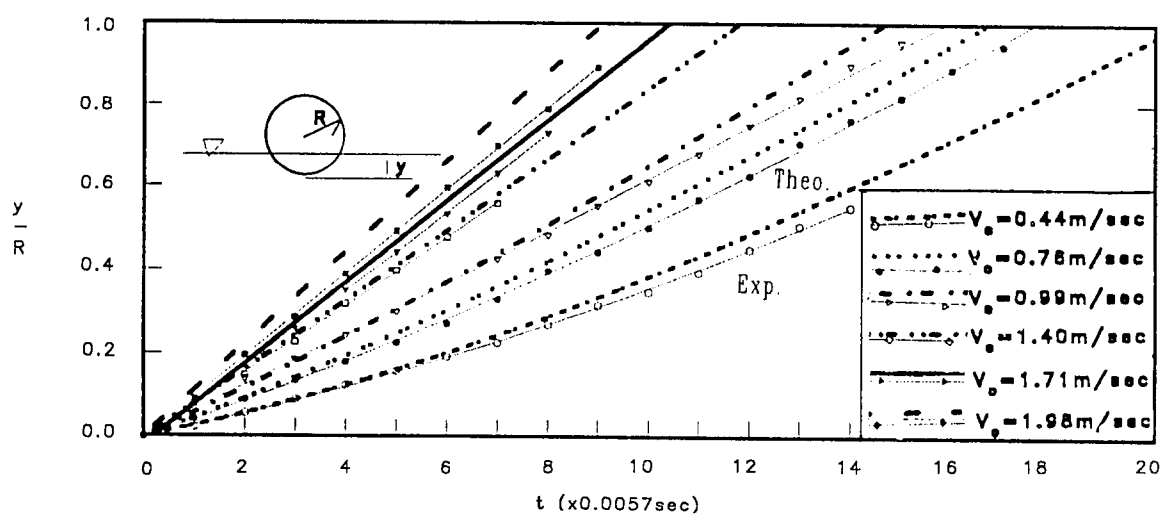

Fig. 8. Comparison between theoretical and experimental results for displacement of cylinder after water impact.

3.2.2. Impact pressure and water surface waveform

After analysis and processing, experimental results for the cylinder indicated that the water surface variation processes have similar steps. Briefly, only the pressure, acceleration and the water surface waveforms (when the impact velocity is 0.767 m/s) are used here to illustrate the details (Fig. 9). The upper right-hand portion of Fig. 9 displays records for pressure and acceleration. The horizontal axis is calibrated to have the same interval of video images (5.7×10^{-3} s). Figs. 9a–9j summarize the results obtained for the water surface waveform. These figures closely correspond to each other.

At the instant of impact pressure $\theta = 0^\circ$ and 7.5° (Fig. 9a), the variation of water surface is slight. At $\theta = 15^\circ$, the water splashes a large spray to impact the object. At $\theta = 30^\circ$, the water surface begins rising along the cylinder surface (Figs. 9d–9e) and the impact pressure no longer exists. Fig. 9e summarizes the results obtained measuring the boundary lines and binarization. Results of different experimental cases indicate that the smaller the impact velocity, the earlier the rising begins. When entry depth further increases, the rising water surface begins to separate from the surface of the cylinder (Figs. 9f–9i). Figs. 9f and 9g present the results after binarization and accumulative addition. The variation of the water surface through eight time stages is next examined. For all the cases in this study, the separation point remains unchanged after separation occurs. Fig. 10 shows the relationship between the mean separation point and the impact velocity, indicating that the higher the impact velocity, the earlier separation begins. When impact velocity is greater than 98 cm/s, the samples have an almost linear distribution. This may be partially owing to constant velocity movement.

3.2.3. The velocity distribution in a flow field

A high-speed CCD camera is used for this study, plastic particles with a gravity ratio of 1.06 and a diameter of 0.2 mm are placed in the flow field. These particles have an extremely low diving velocity and can remain still during the impact. These particles are spread onto a 2 cm sheet. Following the accumulative addition of image records, an approximate cross-section of the flow field particle trace of the water molecular movement can be obtained. After accumulative addition, binarization, and recognition, a vector drawing of the flow field velocity can be made.

Fig. 12 shows the flow field particle traces derived from the accumulative addition. Fig. 12a shows the particle image of the flow field in four time stages of Fig. 11. It is described as the "splashing" effect in Section 3.2.1. This figure reveals only flow field particle traces in time stages c and d during the entire impact; almost no change of flow field particles occurs in the time stages a and b. During those stages, the impact pressure occurs. Fig. 12b shows the effect of "rising along the surface of a cylinder" as described in Section 3.2.1. A certain amount of particles around the cylinder surface become disturbed. However, the particles at the far end remain still. Figs. 12c and 12d illustrate the "separation" described in Section 3.2.1. The cylinder submerges into water and causes a flow of particles. When the entry depth increases, the flow expands from the near to the far end. The particles move throughout the whole observation area; those at the water surface move upward and make the surface rise.

The flow field velocity distribution provides further insight into the difference in characteristics before and after the "separation" effect. In this study, the flow field patterns under various impact velocities are quite similar. Fig. 13 summarizes the results in which the impact velocities are

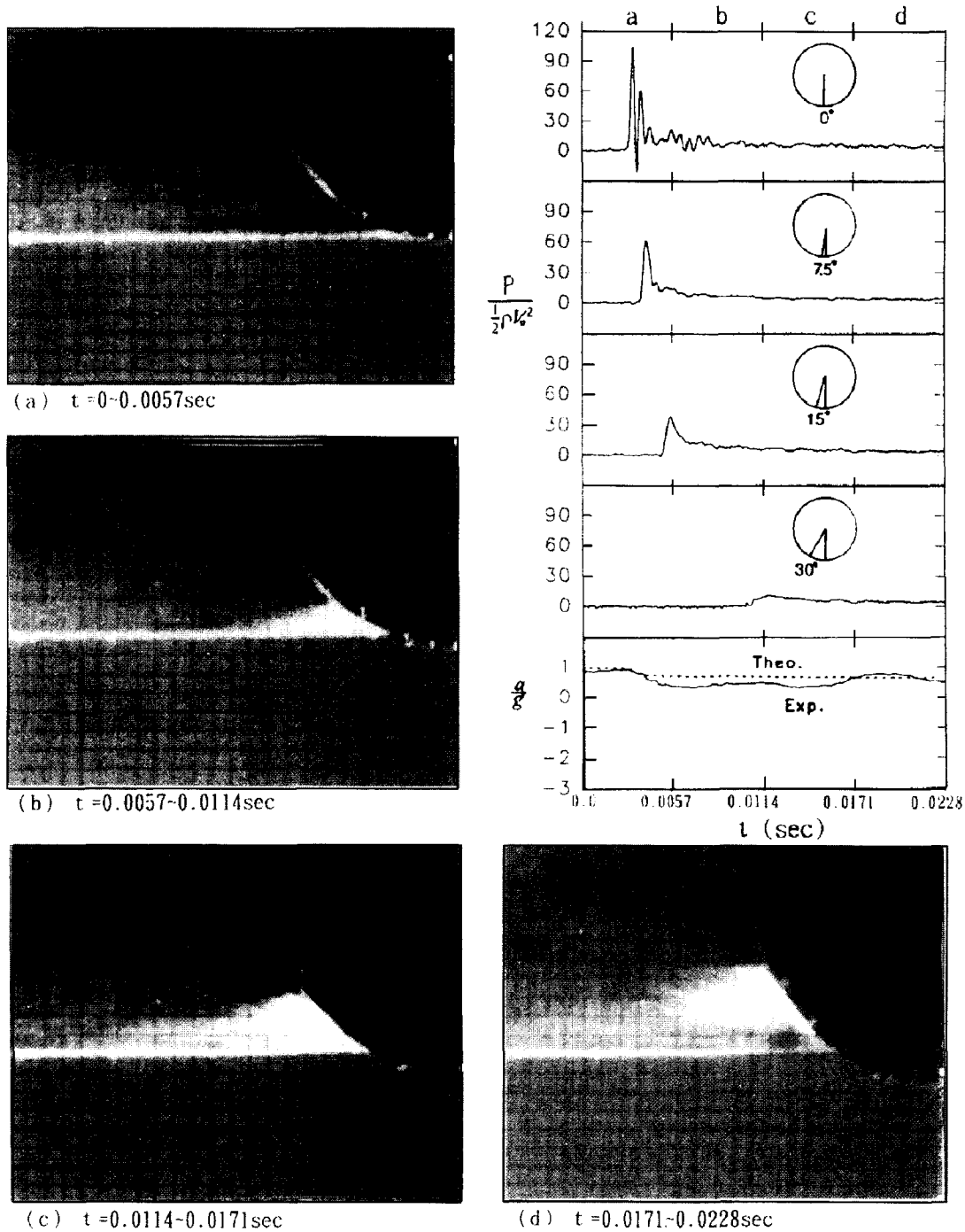

Fig. 9. Dimensionless impact pressure and acceleration records and water surface wave formation of cylinder for water impact.

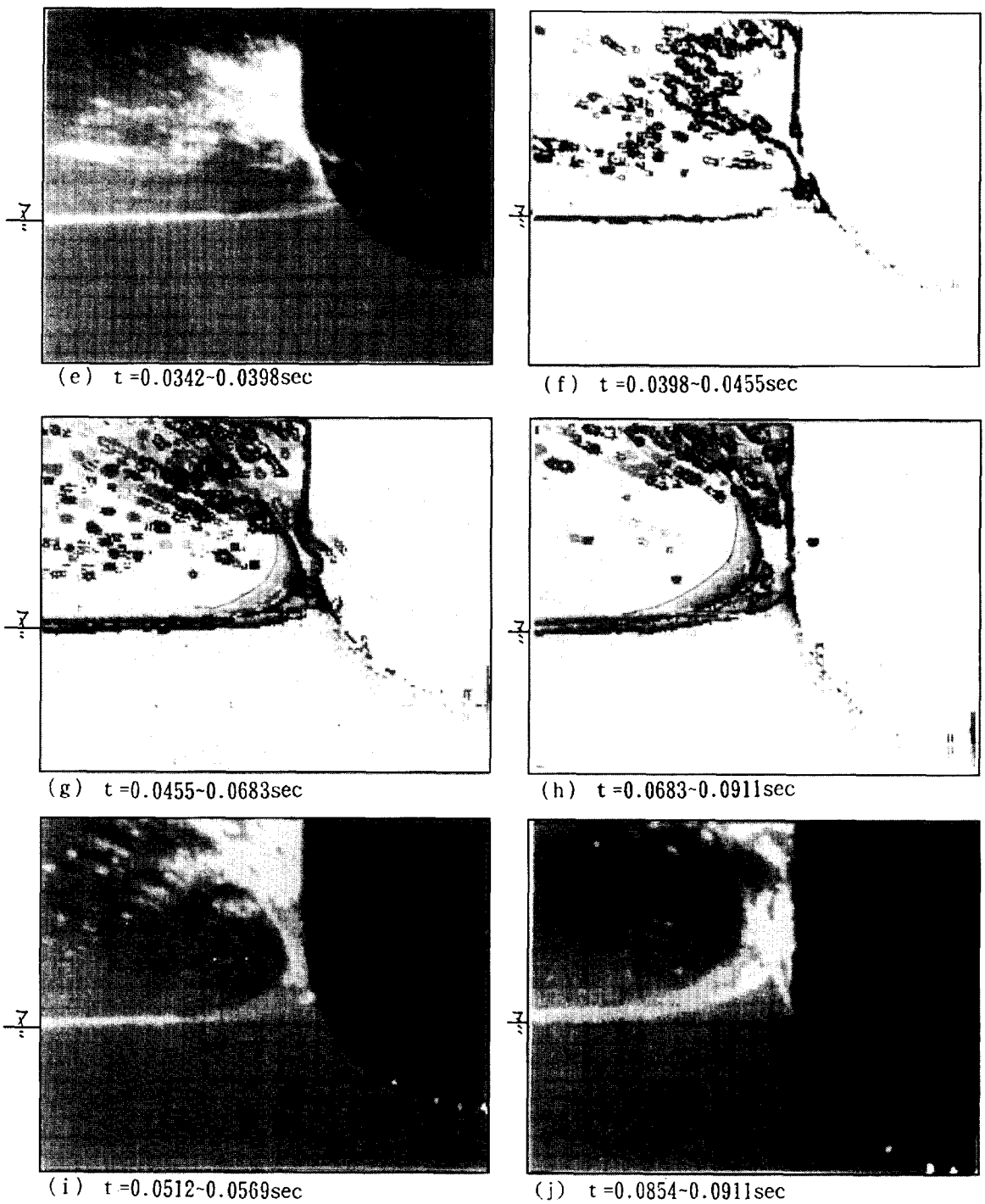

Fig. 9. Continued.

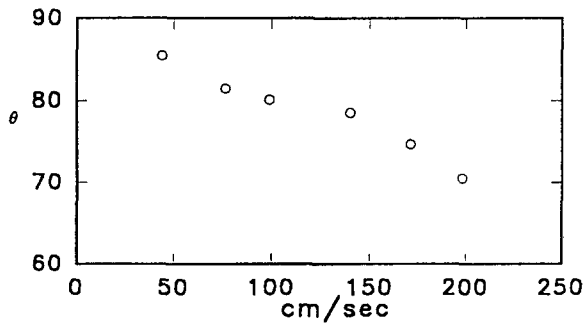

Fig. 10. "Separation point" distribution under various impact velocities.

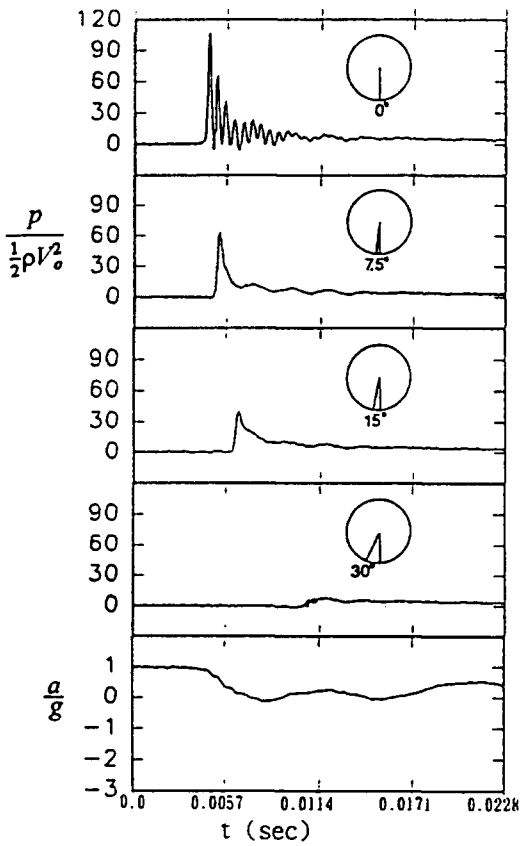

Fig. 11. Dimensionless impact pressure and acceleration records ($V_0 = 98.9$ cm/s).

different. Fig. 13a shows the flow field velocity distribution having just separated. Fig. 13b shows the distribution after separation. Figs. 13c and 13d are the mean results derived from Figs. 13a and 13b. As clearly indicated in these figures, the near cylinder area having a flow is quite small just "separation"; in addition, the rising particles have a higher speed. The flow area becomes large after

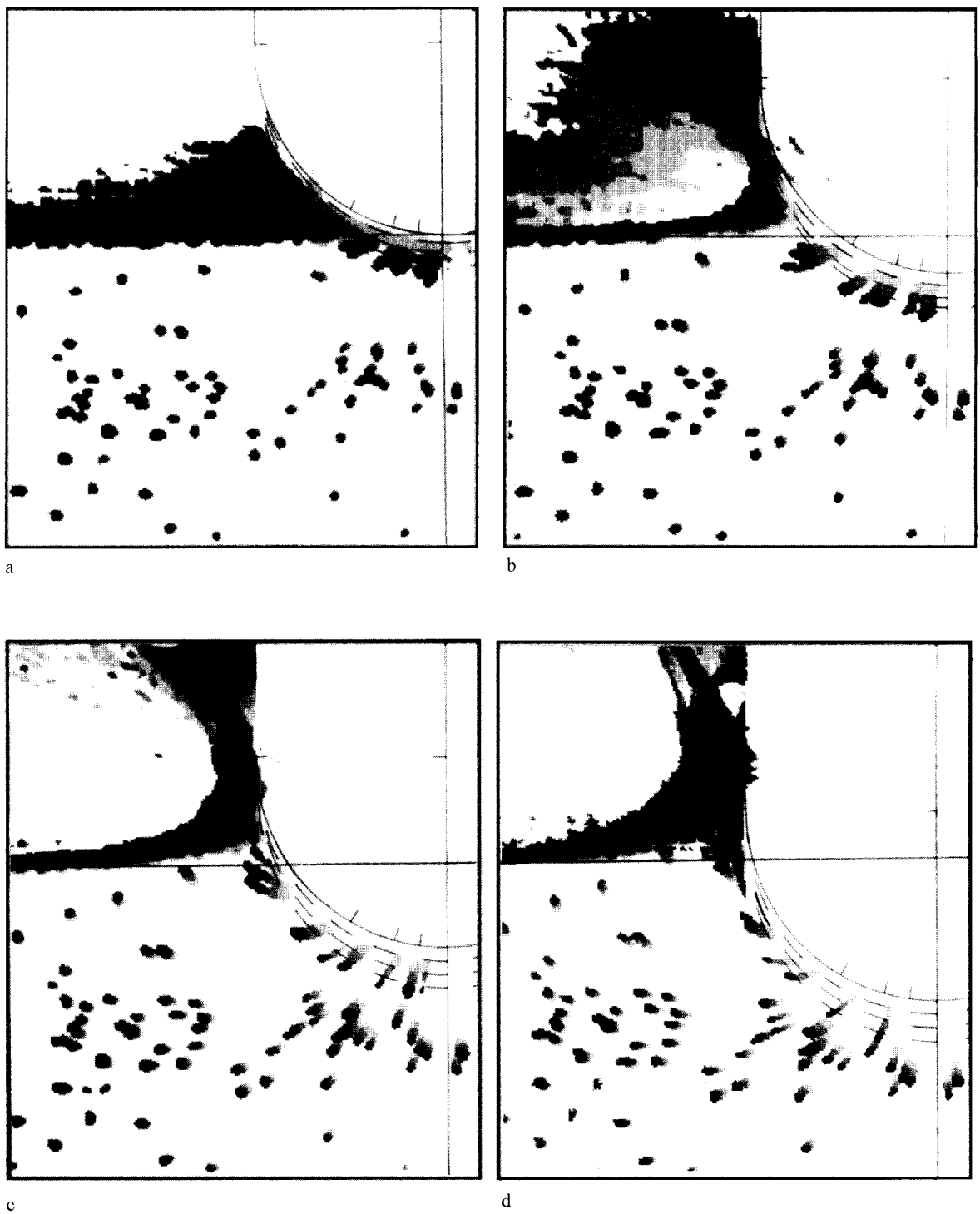

Fig. 12. Flow field particle traces in different time stages: (a) $t = 0$–0.0228 s; (b) $t = 0.0228$–0.0456 s; (c) $t = 0.0455$–0.0683 s; (d) $t = 0.0683$–0.0911 s.

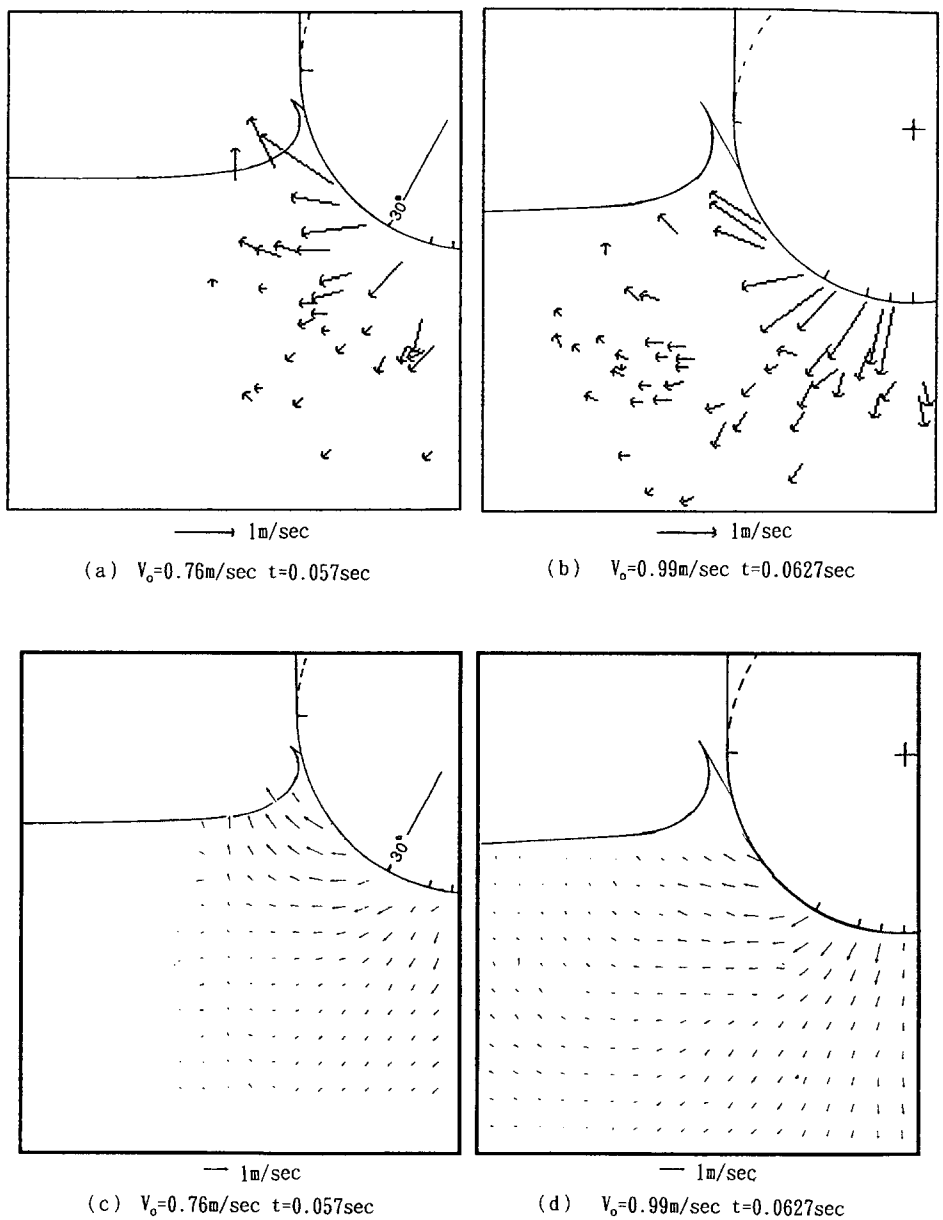

Fig. 13. Flow field velocity distribution: (a) velocity distribution having just separated; (b) distribution after separation; (c and d) the mean results derived from (a) and (b).

"separation" and the particles in the rising part have a more even velocity distribution. These findings can provide valuable information for theoretical and numerical investigations in the future.

3.2.4. Discussion

Until now, we have discussed the physical mechanism of water impact on a cylinder having one diameter. To consider the effect of the model diameter will be necessary. For further investigation, we propose the following steps:

1. Modify the falling mechanism, using hydraulic control and LVDT in control and measure the body velocity accurately.
2. Use different diameter model cylinders to discuss the scaling effect of the pressure gauge on measurement results.
3. Focus on water surface variation for different diameter models, unconditional simultaneous measurement and flow field visualization, we use pause laser light sheet and high-sensitivity, high-density film to investigate the interaction of a solid body and water surface including "rising of water along the surface of the cylinder", "separation", "splashing", and so on.

4. Conclusions

1. This study has mechanically measured and simultaneously observed the flow field. The method provides both high-speed data acquisition and high-sensitivity images. It can be used in observing the interaction between the structure and flow under an unsteady flow field (e.g., breaking waves, turbulent flow). The scheme can find further application once the camera's sensor capability is enhanced.
2. Experimental results indicate the presence of an air layer after the flat-bottom body impacts the water surface. The air layer causes the pressure distribution in the interior of the flat-bottom to be uniform. The pressure on the edge changes more frequently owing to the occurrence of bubbles. The primary reason for pressure oscillation is not the horizontal vibration of sound waves in the air layer, but instead air layer compression and expansion.
3. The early stages of impact of a cylinder cause a change in the water surface that can be divided into three phases: the "splashing" effect, the "rising along the cylinder surface" effect, and the "separation" effect. Impact pressure occurs only in the "splashing" effect. Increasing the impact velocity causes (a) the separation of a rising water surface to occur earlier and (b) the water surface near the cylinder to have more obvious rising effect. During the "splashing", there is almost no water particle flow in the flow field. When the entry depth increases, the water particles expand to the far end. This study provides a complete mechanical structure to construct a numerical model in a future investigation.

Appendix A. Cause of pressure oscillation

It is possible that the oscillation may be caused by compressing and expanding an air layer. Fig. 14 presents the physical model under the assumption of isothermal condition, where M is the mass of a flat-bottom body, m added mass, X_1, X_2 movement distance, h, h_0 air layer thickness, P pressure, and P_0 initial pressure (atmospheric pressure).

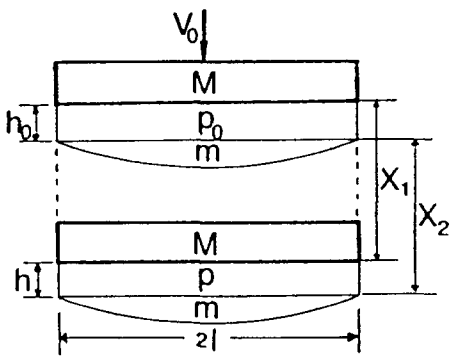

Fig. 14. Physical model of flat-bottom body for water impact.

The initial condition is

$$t = 0, \quad X_1 = 0, \quad \frac{dX_1}{dt} = V_0,$$

$$X_2 = 0, \quad \frac{dX_2}{dt} = 0. \tag{A.1}$$

The added mass of unit length for the flat-bottom body is

$$m = \frac{\pi l^2 \rho_w}{2}, \tag{A.2}$$

where l is the half-width of the flat-bottom body.

Momentum equations are

$$M \frac{d^2 x_1}{dt^2} = -2l(p - p_0), \tag{A.3}$$

$$m \frac{d^2 x_2}{dt^2} = 2l(p - p_0), \tag{A.4}$$

By the geometry of Fig. 14,

$$\frac{d^2 x_1}{dt^2} = \frac{d^2 x_2}{dt^2} - \frac{d^2 h}{dt^2}. \tag{A.5}$$

Substituting Eqs. (A.3) and (A.4) into (A.5) gives

$$\frac{d^2 h}{dt^2} = \left(\frac{M + m}{Mm}\right) 2l(p - p_0). \tag{A.6}$$

Using $Ph = P_0 h_0$, Eq. (A.6) becomes

$$\frac{d^2 h}{dt^2} = \left(\frac{M + m}{Mm}\right) 2lp_0 \left(\frac{h_0}{h} - 1\right). \tag{A.7}$$

Expanding the variation rate of h in Eq. (7), we obtain

$$\frac{d^2\eta}{dt^2} = -v^2(\eta + \eta^2 + \eta^3 + \cdots), \tag{A.8}$$

where

$$v^2 = \left(\frac{M+m}{Mm}\right)\frac{2l}{h_0}p_0. \tag{A.9}$$

For $\eta < 1$, take a first-order similar solution

$$\eta = q\sin(vt + \phi) \tag{A.10}$$

caused by $ph_0(1-\eta) = p_0h_0$,

$$p = \frac{p_0}{1-\eta} = (1 + \eta + \eta^2 + \eta^3 + \cdots)P_0. \tag{A.11}$$

Therefore, the main oscillation frequency produced by air layer compression and expansion is $f = (v/2\pi)$. Using Eq. (A.9), this becomes

$$f = \frac{1}{2\pi}\sqrt{\left(\frac{M+m}{Mm}\right)\frac{2l}{h_0}P_0}. \tag{A.12}$$

The air layer thickness is

$$h_0 = \left(\frac{M+m}{Mm}\right)\frac{2lP_0}{4\pi^2f^2}. \tag{A.13}$$

Appendix B. Momentum equations and added mass after impact

Only a two-dimensional, incompressible, non-viscous fluid still in initial conditions is considered in calculating the relationships between velocity and time after impact with water. Based on the law of conservation of momentum, we obtain

$$M\frac{dV}{dt} + \frac{d}{dt}(mV) = q, \tag{B.1}$$

where M is the mass of falling body per unit length, m the added mass after impact, V the velocity after impact with water, t the time, and q the external force after impact with water (e.g., gravity, buoyancy). Therefore, the impact force caused by added mass after impact with water should be

$$F = \frac{d}{dt}(mV) = m\frac{dV}{dt} + V\frac{dm}{dt} = m\frac{dV}{dt} + V\frac{dm}{dy}\frac{dy}{dt} = m\frac{dv}{dt} + V^2\frac{dm}{dy}. \tag{B.2}$$

To solve Eqs. (B.2) and (B.3), the relation between added mass and entry depth y must be known. Taking the conformal mapping from Taylor (1930) as a reference yields the following result:

$$\frac{m}{\rho\pi R^2} = \frac{\pi^2}{3}\frac{1-\cos\alpha}{(2\pi-\alpha)} + \frac{1-\cos\alpha}{6} + \frac{\sin\alpha-\alpha}{2\pi}, \tag{B.3}$$

where

$$\frac{\alpha}{2} = \cos^{-1}\left(\frac{R-y}{R}\right), \quad 0 \leqslant y \leqslant R$$

(R is the radius of the cylinder; y is the entry depth of the cylinder).

For a cylinder, the external force, q, can be represented by the resultant of gravity and buoyancy, i.e.,

$$q = Mg - \left\{\frac{\pi R^2}{2} - R^2\sin^{-1}(1-r) - R^2(1-r)\sqrt{2r-r^2}\right\}\rho_w g, \tag{B.4}$$

where $r = y/R$, the ratio of entry depth to the radius of the cylinder. Substituting (B.2), (B.3) and (B.4) into (B.1) yields a second-order non-linear ordinary differential equation. Moreover, the relationships of displacement velocity and acceleration can be calculated via the Runge–Kutta method.

References

von Karman, T. (1929) The impact of seaplane floats during landing, NACA TN321, October, Washington.

Campbell, I.M.C. and P.A. Weynberg (1980) Measurement of parameters affecting slamming. Final report, Wolfson Unit for Marine Tech. Rep. No. 440, Technology Reports Center No. OTR-8042.

Chuang, S.L. (1966) Experiments on flat-bottom slamming, J. Ship Res. 10, 10–17.

Chuang, S.L. (1970) Investigation of impact of rigid and elastic bodies with water, NSRDC Rep. 3248, February.

Fujita, Y. (1953) On the impulsive pressure of circular plate falling upon a water-surface (2nd report), J. Soc. Naval Architects in Japan 94, 105–110.

Gerlach, C.R. (1968) Investigation of water impact of blunt rigid-bodies-size scale, Technical Report No. 2, Contract No. N00014-67-C-213, Southwest Research Institute, No. V.

Greenhow, M. and W.-M. Lin (1983) Non-linear free surface effects. Experiment and theory, Rep. No. 83-19, unpublished report, Department of Ocean Engineering, MIT.

Greenhow, M. (1988) Water-entry and exit of a horizontal circular cylinder, Appl. Ocean Res. 10, 191–198.

Imaich, K. and K. Ohmi (1983) Numerical processing of flow-visualization pictures – measurement of two dimensional vortex flow, J. Fluid Mech. 129, 283–311.

Khalighi, K. and Y.H. Lee (1989) Particle tracking velocimetry: an automatic image processing algorithm, Appl. Opt. 28, 4332a.

Koehler, B.R. and C.F. Kettleborough (1977) Hydrodynamic impact of a falling body upon a viscous incompressible fluid, J. Ship Res. 21, 165–181.

Miyamoto, T. and K. Tanizawa (1984) A study of the impact load on ship bow, J. Soc. Naval Architects, Japan, 156, 297–305.

Naccalhe, N.J. and R. Shimghal (1984) SPTA: a proposed algorithm for thinning binary patterns, IEEE Trans. Systems Man Cybernet. SMC-14, 409–418.

Ng, C.O. and S.C. Kot (1992) Computations of water impact on a two-dimensional flat-bottomed body with a volume-of-fluid method, Ocean Eng. 19, 377–393.

Taylor, J.L. (1930) Some hydrodynamic inertia coefficients, Philos. Mag. (Series 7) 9, 161–183.
Verhagen, J.H.G. (1967) The impact of a flat plate on a water surface, J. Ship Res. 11, 211–223.
Whitman, A.M. and M.C. Pancione (1973) A similitude relation for flat-plate hydrodynamic impact, J. Ship Res. 17 (3), 38–42.
Wagner, H. (1932) Uber Stoss-und Gleitvorgange an der Oberflache von Flussigkeiten, ZAMM 12, 193 (see also Phenomena of Impact and Planning on Water, NACA, Translation 1366).